HAL
open science

Force Density Improvements from Increasing the Number of Airgap Surface in Synchronous Linear Actuators

Pierre-Emmanuel Cavarec, Hamid Ben Ahmed, Bernard Multon

To cite this version:

Pierre-Emmanuel Cavarec, Hamid Ben Ahmed, Bernard Multon. Force Density Improvements from Increasing the Number of Airgap Surface in Synchronous Linear Actuators. IEE Proceedings Electric Power Applications, 2003, Vol.150 (n°1), pp.106-120. 10.1049/ip-epa:20020628 . hal-00674672

HAL Id: hal-00674672

https://hal.science/hal-00674672v1

Submitted on 27 Feb 2012

HAL is a multi-disciplinary open access archive for the deposit and dissemination of scientific research documents, whether they are published or not. The documents may come from teaching and research institutions in France or abroad, or from public or private research centers.

L'archive ouverte pluridisciplinaire **HAL**, est destinée au dépôt et à la diffusion de documents scientifiques de niveau recherche, publiés ou non, émanant des établissements d'enseignement et de recherche français ou étrangers, des laboratoires publics ou privés.

IEE Proc-Elec. Power Appl. Yol.150, n°1, january 2003, pp.106-120

Force Density Improvements from Increasing the Number of Airgap Surfaces in Synchronous Linear Actuators

P.E. Cavarec, H. Ben Ahmed, B. Multon

Laboratoire d'Electricité, Signaux et Robotique (LESiR, ESA CNRS 8029)
ENS de Cachan - Brittany Branch
Campus de Ker Lann, 35170 BRUZ France

e-mail: cavarec@bretagne.ens-cachan.fr

Abstract: This paper presents a realistic comparison of several electromagnetic architectures for high force density actuators. Four equivalent architectures are chosen and computed with a two-dimensional finite element model. For each architecture, size is optimised in order to maximise the force-volume ratio. This optimisation step is performed with a fixed mechanical airgap. A thermal model is then used to calculate the current density in the coils. Results show that global-coil architecture performance increases more sharply than other architectures; a scaling effect is thereby introduced for global-coil architectures. A global-coil multi-airgap actuator is presented to illustrate the theoretical results.

1. INTRODUCTION

It is quite frequent, especially for direct-drive applications, to require high force density actuators (e.g. electrical jacks, robot arms, integrated wheel-motors).
Normally, whenever torque or force needs to be produced at a minimum threshold, either the number of poles is increased or the polar step is reduced in order to minimise the volume and mass of the magnetic circuit. However, the physical limitations of airgap magnetic shear stress cannot be overcome: this stress gets limited by means of both airgap induction and magnetic field density in the armature currents. Airgap induction, in turn, is limited by the saturation of ferromagnetic materials and the field is limited by heating and/or the demagnetisation of any permanent magnets used for excitation. The maximum attainable values of airgap magnetic shear stress rarely exceed 10 N/cm². An actuator can thereby be summarised as a system for producing magnetic fields that interact inside an airgap where magnetic stress is generated.
Another approach, conceived some twenty years ago [1,2] yet still rather undeveloped due to its conceptual complexity, consists of splitting the active zone so as to increase airgap surfaces, thus giving rise to what are called "multi-airgap structures".
In order to demonstrate the advantages of this concept, we will draw a comparison of the evolution of several architectures, in an effort to highlight the value of global-coil multi-airgap structures. An example of a specific configuration will be presented afterwards [3].

2. SEVERAL PERMANENT MAGNET ARCHITECTURES

We have chosen four kinds of permanent magnet linear architecture. Each represents one phase of a real actuator. An entire actuator is composed of three independent phases. Theses phases are identical. They are placed along the same mobile parts and are separated by one third of the step.
This section is devoted to presenting these particular architectures.

2.1 THE BASIC SINGLE-AIRGAP ARCHITECTURE

This first architecture remains the most conventional: the single-airgap architecture, with a surface-mounted permanent magnet. Compared to the standard rotative architecture, the main difference lies in the separation between phases. All phases herein are completely independent of one another.

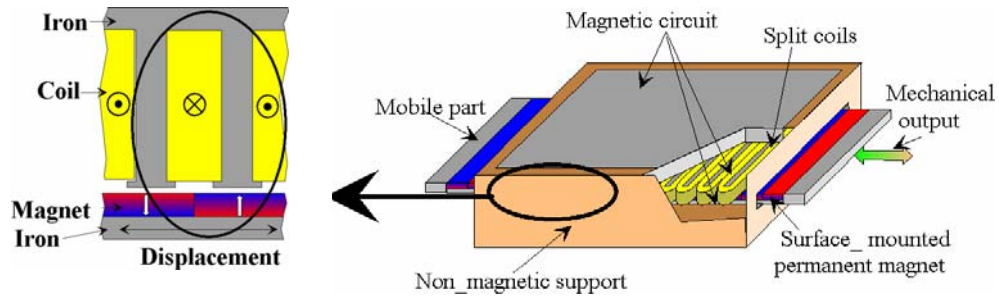

Fig. 1: Basic single-airgap architecture (1) and 3D view of one phase of an actuator

2.2 THE MULTI-MOTOR ARCHITECTURE

The second architecture is based on the classical single-airgap actuator, with differences stemming from the fact that not just one but several mobile parts are acting in parallel. It can be stated that the poly-discoid architecture is developed from the same structure, yet the phases are not separated from one another.

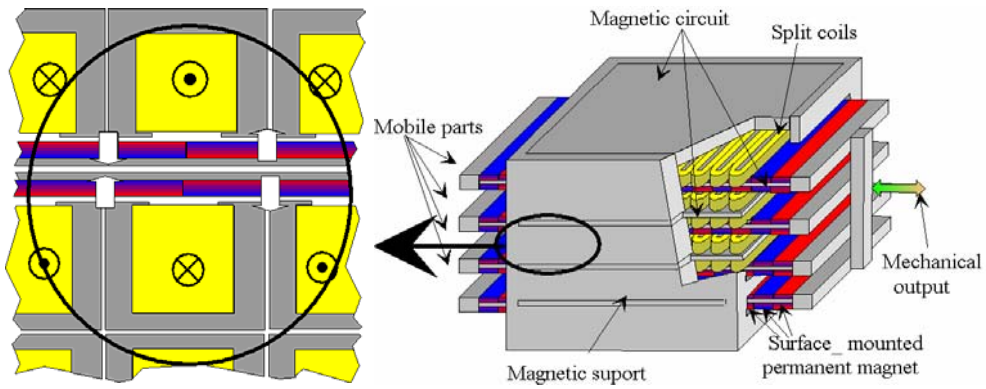

Fig. 2: Multi-motor architecture (2) and 3D view of one phase of an actuator

2.3 THE SPLIT-COIL MULTI-AIRGAP ARCHITECTURE

The third architecture is similar to that of the multi-motor, except for the flux return circuit. The back-iron has been eliminated from both the internal moving elements and the internal split-coil part. For the same given force, actuator volume with this type of architecture is decreased. This particular structure has been proposed in [4].

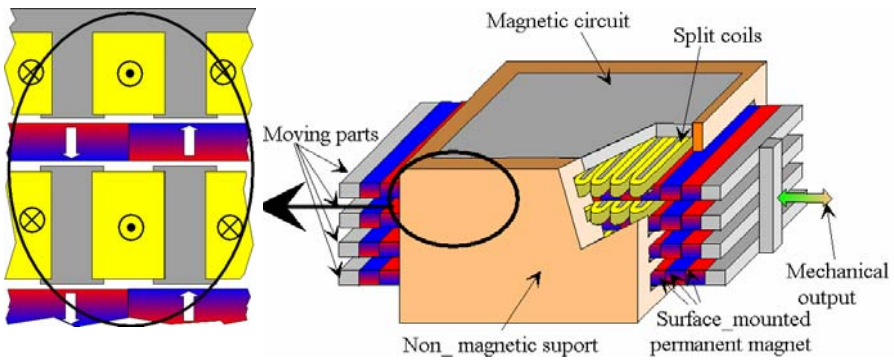

Fig. 3: Split-coil multi-airgap architecture (3) and 3D view of one phase of an actuator

2.4 THE GLOBAL-COIL MULTI-AIRGAP ARCHITECTURE

Lastly, the global-coil multi-airgap architecture is based on the same surface-mounted permanent magnet parts. A single global coil is used for all airgaps; only one global coil per phase however is present. Two configurations are possible: either mobile or fixed permanent magnets.

The mobile-magnet solution (see Fig. 4a) is close to that of the previous architecture.

The fixed-magnet solution (Fig. 4b) features passive mobile parts that require fewer permanent magnets. Moreover, iron losses are mainly localised inside the magnetic part. In this mobile-iron solution, the cooling step is made easier.

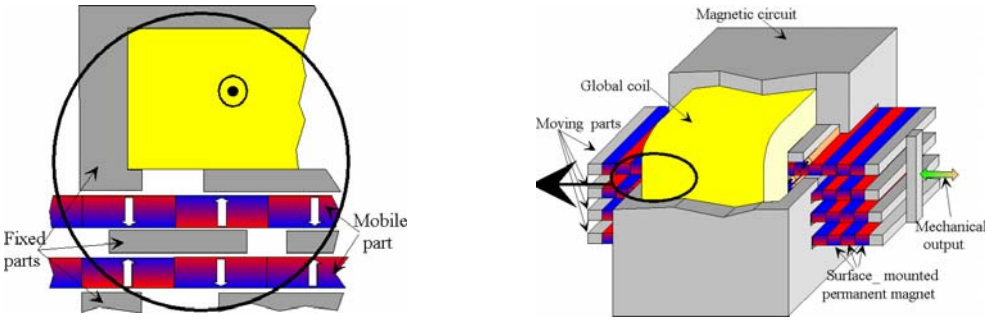

Fig. 4a: Global-coil multi-airgap architecture (4) and 3D view of one phase of an actuator with mobile permanent magnets

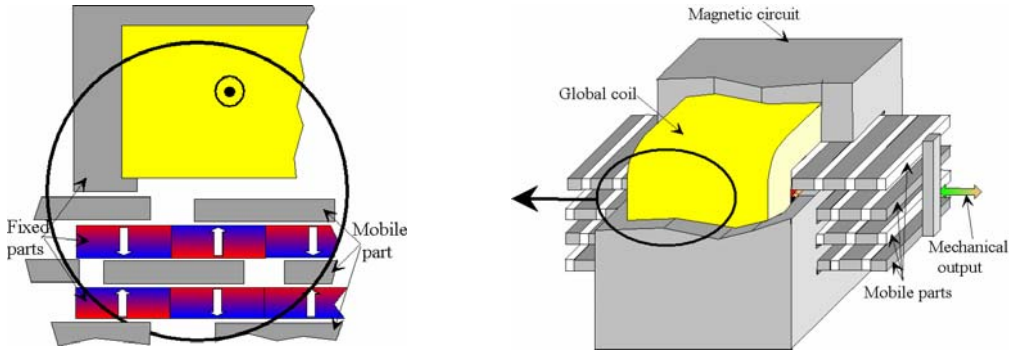

Fig. 4b: Global-coil multi-airgap architecture (4) and 3D view of one phase of a fixed permanent magnet actuator

This set-up has been made possible by a “longitudinal flux”. The following figures illustrate the difference between the “longitudinal flux” and “transverse flux” concepts.

- The split-coil multi-airgap architecture exhibits transverse flux, which means that the flux moves from a given airgap to the opposite one. Figure 5a illustrates transverse flux for reluctance architecture.

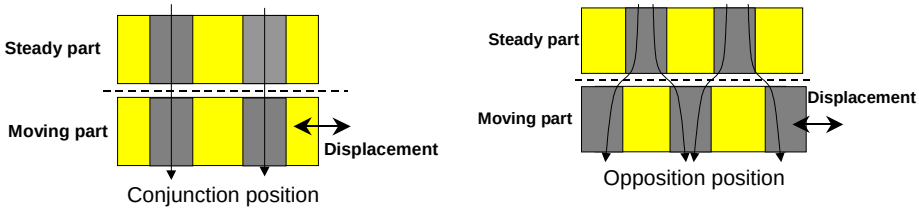

Fig. 5a: Transverse flux reluctance architecture

- The global-coil multi-airgap architecture, on the other hand, has longitudinal flux, which means that the flux follows the airgap surface. Figure 5b illustrates longitudinal flux for reluctance architecture [7].

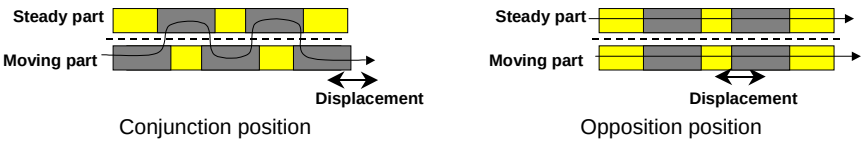

Fig. 5b: Longitudinal flux reluctance architecture

3. ARCHITECTURE OPTIMISATION FOR MAXIMUM FORCE

In order to compare the four architectures discussed above, each is to be optimised under identical conditions. The models used for each optimisation exercise must be both accurate and simple (in order to keep computation time within reasonable limits). The magnetic models are based on Saturated Finite Element Models, while the thermal models are equivalent electrical models. All optimisation parameters have been minimised.

3.1 THE FINITE ELEMENT METHOD FOR CLASSICAL ARCHITECTURES

We have decided to focus on just one actuator phase, an approach made possible thanks to the magnetic independence of the phases.
The first three architectures (i.e. the basic single-airgap architecture, the multi-motor architecture and the split-coil multi-airgap architecture) may be modelled in terms of simple 2D characteristic regions, as illustrated in Figure 6.

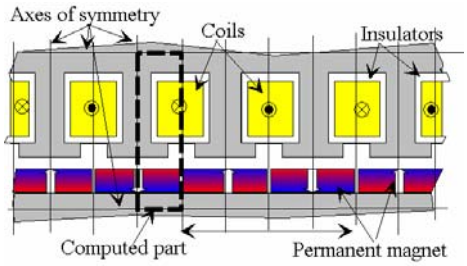

Fig. 6: A portion of the multi-motor architecture with the 2D Finite Element-modelled part (see Figure 2)

Using such an element, the actuator step τ is four times its width. Flux remains parallel to the high, low and left sides while normal to the right side.

3.2 THE FINITE ELEMENT METHOD FOR GLOBAL-COIL ARCHITECTURE

As far as global-coil architecture is concerned, it is not possible to simulate an entire actuator. The flux conservation rule is used to model the return part of the flux.
By making use of axes of symmetry, the area for computation may be decreased.

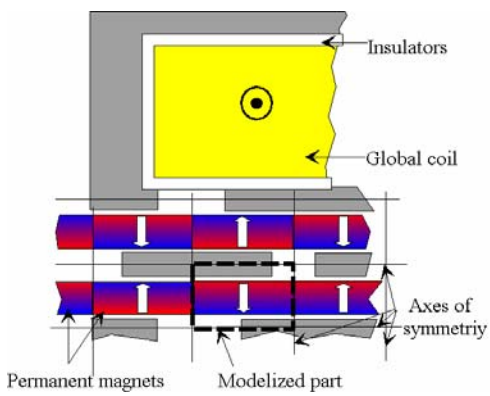

Fig. 7: Axes of symmetry for the global-coil multi-airgap actuator

Using such an element, the actuator step τ is twice the pattern width. Flux remains parallel to the high and low sides and moves from the right side to the left side.

3.3 MODEL OF MAGNETIC MATERIAL CHARACTERISTICS

We have developed a non-linear model of the magnetic iron based on an analytical approximation of the B(H) curve, as follows:

$$\mu_r(H) = 1 + \frac{B_{sat.}}{\mu_0.H}.\arctan\left(\frac{\mu_0.(\mu_{r_\max} - 1).H}{B_{sat.}}\right) \qquad (1)$$

The magnetic curves are shown in the following figures.

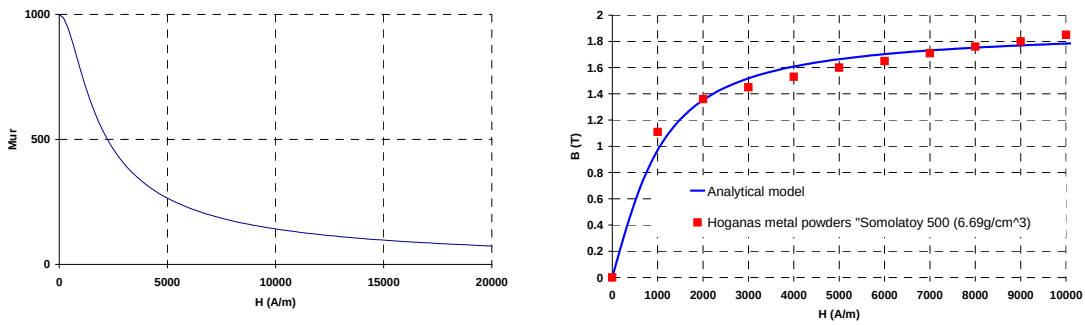

Fig. 8: Relative permeability curve and saturated B(H) curve for Hoganas® SOMALOY 500 soft magnetic composites (parameters of the model are : $B_{sat} = 1.6T$ and $\mu_{r\max} = 1000$)

These magnetic values have been chosen as close as possible to those of soft magnetic composites, for which iron losses are low.

3.4 THE MECHANICAL FORCE COMPUTATION

The aim of these finite element computations is to compare force-volume ratios among the various architectures presented in Section 1.
The average force can be computed on the basis of the flux/nI diagram for square-wave current (in phase with flux variation) [8]. This choice allows computing the force solely with the conjunction flux curve.

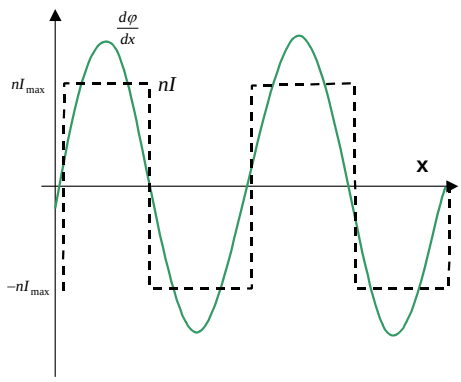

Fig. 9a: Square-wave current

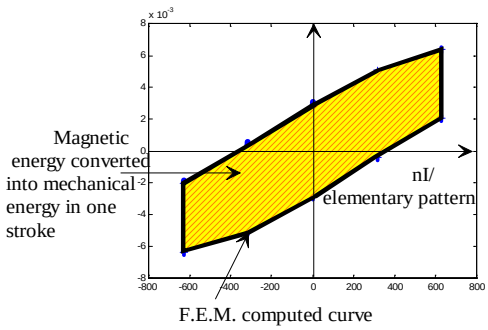

Fig. 9b: Global energy conversion cycle for one elementary pattern

The area W_m of the cycle represents the transfer from electrical energy to mechanical energy at each step τ of the actuator. In the case of the ideal square-current supply, we obtain:

$$W_m = 2.\int_{nI_{\min}}^{nI_{\max}} \varphi(nI).dnI \qquad \text{(see Fig. 9b)}$$

where nI is the magneto-motive force per pattern and φ the finite element-computed flux per pattern.

The average force $\overline{f}$ of an elementary pattern is equal to the mechanical energy divided by the step:

$$\overline{f} = \frac{W_m}{\tau} \qquad (2)$$

The total force $\overline{F}$ of the actuator is the sum of the elementary pattern forces (N_s in series and N_p in parallel) for the q phases:

$$\overline{F} = \sum \overline{f} = q.n_p.n_s.\overline{f} \quad (3)$$

$$\overline{F} = q.N_p.N_s.\frac{W_m}{\tau} \quad (4)$$

N.B.: For unsaturated actuators with a null phase between the EMF and the current, the transferred energy can be easily calculated as follows:

$$W_m = k.\varphi_{magnet}.nI_{\max} \quad (5)$$

with:

φ_{magnet} : the magnetic flux of the pattern when the current is null;

$nI_{\max}$: the maximum value of the magneto-motive force applied to the pattern;

k (the form coefficient): $k = 4$ with a square-wave current, and $k = \pi$ with a sine wave current and flux.

3.5 THE THERMAL MODEL

One major difficulty in carrying out such a comparison is the complexity of the thermal model: the magneto-motive force (nI) of the elementary pattern is directly limited by the copper losses that can be extracted from the actuator.

We have chosen the case of airflow-cooling actuators within a steady-state study.
In an initial approach, we considered homogeneous temperatures in both the copper and iron materials, which supposes very low thermal resistance inside the copper and iron areas.

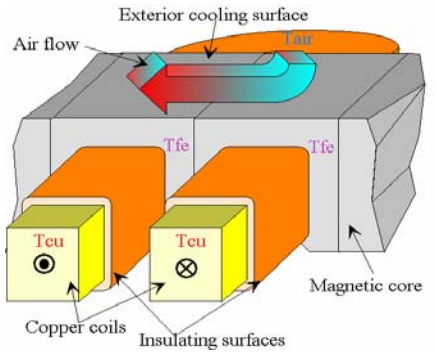

Fig. 10a: The thermal model

At lower frequencies, especially in generating force with a low-speed actuator, we neglected iron losses. However, the magnetic material model has been set up to yield low iron losses (soft magnetic composite, see Fig. 8).

With a square-wave current, we obtain:

$$P_{cu} = \rho_{cu}.J_{\max}{}^2.V_{cu} \quad (6)$$

Under constant thermal conditions:

$$P_{cu} = \frac{\lambda_i.S_i.(T_{cu} - T_{fe})}{D_i} \quad (7)$$

and:

$$P_{cu} = \lambda_e.S_e.(T_{fe} - T_{air}) \quad (8)$$

with:

P_{cu} : overall copper losses,

ρ_{cu} : electrical resistivity of the copper,

$J_{\max}$: maximum current density inside the copper coil,

V_{cu} : copper volume,

λ_i : thermal resistivity of the insulator (in $W.K^{-1}.m^{-1}$),

S_i : surface area of the insulator between the copper and the core,

D_i : insulator thickness,

λ_e : thermal dissipation coefficient of the external surface for convection and radiation (in $W.K^{-1}.m^{-2}$),

S_e : external surface area,

T_{cu} : coil temperature,

T_{fe} : core temperature,

T_{air} : air temperature.

We can sum up the thermal model by means of a simple circuit:

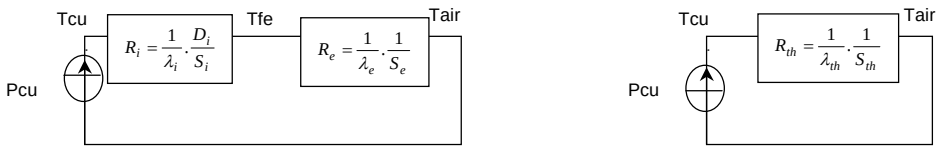

Fig. 10b: Equivalent electrical model and simplified electrical model

3.6 THE GLOBAL DIMENSIONS

Optimisation has been performed with a global square section, which means that actuator height H must be equal to actuator width W. The number of patterns in series N_s constitutes an optimisation parameter. Hence, we obtain:

$$H = h_{pattern}.Ns$$

$$W = H$$

However, length L has not been directly constrained; instead, it depends on the global volume V :

$$L = \frac{V}{L.W}$$

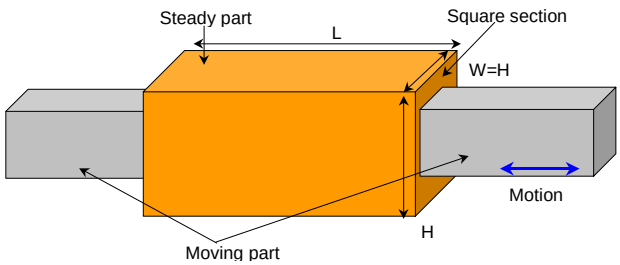

Fig. 11: Shape of square-section actuators

3.7 THE PATTERN'S DIMENSIONAL PARAMETERS FOR CLASSICAL ARCHITECTURES

The so-called “classical architectures” refer to the first three presented above: single-airgap, multi-motor and split-coil. These architectures display a number of overlapping features and can be optimised with just about the same dimensional parameters.

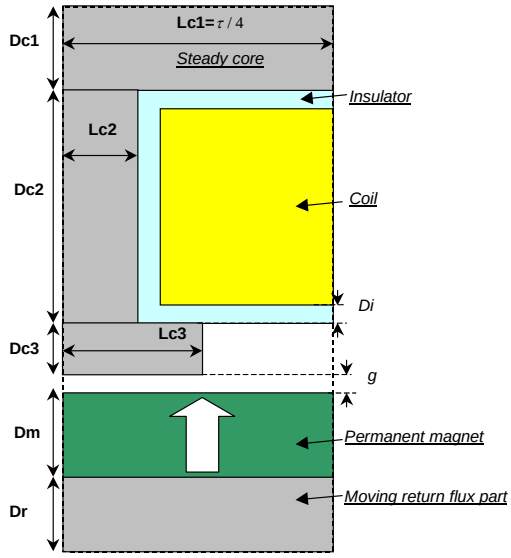

Fig. 12: The geometrical parameters of a pattern

For single-airgap architectures, all dimensional parameters, except for airgap thickness g and insulator thickness Di, are variables.

For multi-motor architectures, it is necessary to add another variable: the number of patterns in parallel (Np). We can then calculate the number of patterns in series with both the global volume and pattern volume.

For split-coil architectures, the parameter Dc1 disappears due to the absence of back iron.

3.8 PATTERN SIZES FOR GLOBAL-COIL ARCHITECTURES

For global-coil architectures, the variables are separated into two categories: geometric dimensions of the pattern, and global dimension ratios.

The pattern geometry variables consist of:

- Dc1: thickness of the magnetic part
- Lc1: length of the magnetic part
- Dm: thickness of the magnet
- Lm: length of the magnet (half-step).

The global dimension ratios are:

- $R_{LH} = \dfrac{L}{H}$: length-to-height ratio
- $R_{CuH} = \dfrac{D_{cu}}{H}$: coil thickness-to-height ratio.

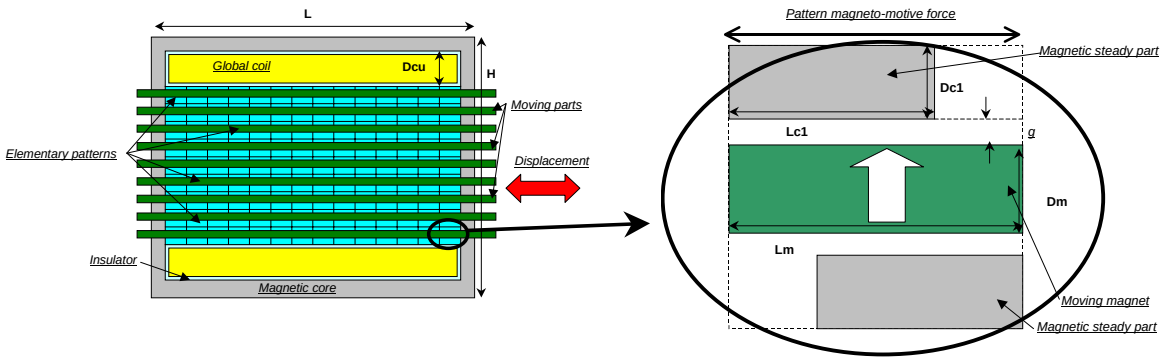

Fig. 13: Global dimensions and pattern dimensions

3.9 THE OPTIMISATION ALGORITHM

The aim of the search algorithm is to optimise each of the various architectures. In order to obtain a feasible architecture, the airgap is maintained at a constant value (1 mm), which is closely related to the mechanical technology exhibited by the actuators (accuracy and guidance). Under these conditions, comparisons prove to be realistic.

Geometrical optimisation is difficult due to the number of unrestricted parameters (up to 6). Hence, the efficiency of classical optimisation is limited as a result of local optima; we have employed a genetic algorithm based on the natural selection process. The initial population has been set at 300. For 200 generations, the computation time for each optimisation is around 4 hours.

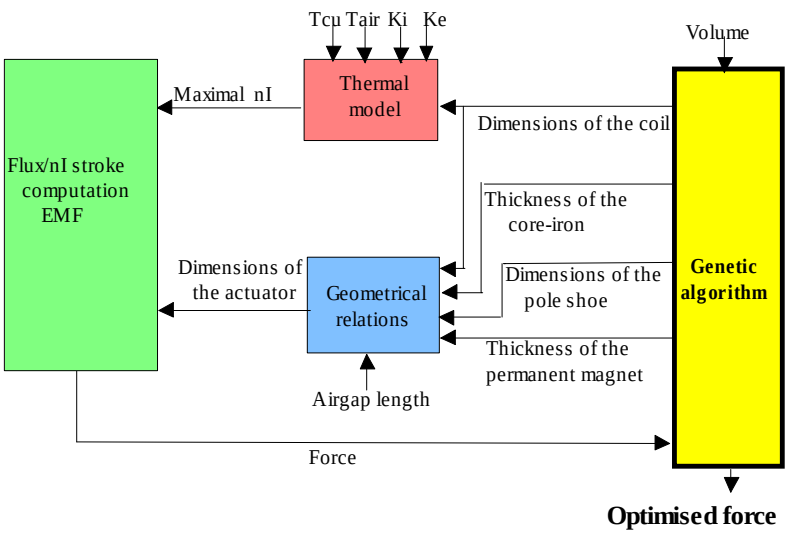

Fig. 14: Global diagram of the optimisation algorithm

4. OPTIMISATION RESULTS

4.1 THE OPTIMISATION PARAMETERS

The selected optimisation parameters can be summed up as follows:

λ_i :	thermal resistivity of the insulator	0.15 W/°C.m (oily paper)
λ_e :	thermal dissipation coefficient	10 W/°C.m^2 (natural airflow cooling)
T_{cu} :	temperature of the copper	120°C
T_{air} :	air temperature	20°C
Di :	thickness of the insulator	1 mm
g :	thickness of the airgap	1 mm
$Bsat$:	saturation magnetic flux density of the magnetic material (see the soft magnetic composite in Fig. 8)	1.6-T
$\mu_{r_\max}$:	maximum relative magnetic permeability	1,000
Br :	remanent induction of the magnet	1-T

Table of parameter values

4.2 OPTIMISATION OF THE CLASSICAL ARCHITECTURES

Using these parameters, we optimised the set of volume-independent values; results are displayed in the following table:

Variable	Single-airgap architecture	Multi-motor architecture	Split-coil architecture
Dc1 (mm)	1.9	1.8	×
Lc1 (mm)	4.7	5.1	5.5
Dc2 (mm)	12.0	12.0	12.1
Lc2 (mm)	1.9	1.9	2.2
Dc3 (mm)	0.9	0.9	2.2
Lc3 (mm)	4.0	4.4	4.7
Dm (mm)	2.8	2.9	3.1
Dr (mm)	2.3	2.4	
Ns		2	2
Coil thickness (mm)	10	10	10.1
Coil length (mm)	3.6	4.4	4.6
Step τ (mm)	18.8	20.5	22.1
Current density J (A/mm^2)	5.2	5	4.9
Core temperature T_{fe} (°C)	115	115	115
Force-volume ratio (N/dm^3)	389	424	476

Table of classical architecture results

The first point to be made is that for both the multi-motor and split-coil architectures, only two patterns in parallel can be observed, which indicates that the optimised actuators contain only one moving part surrounded by two fixed parts. This feature is due to the thermal model, in which the primary thermal resistance is the external one. These architectures are aimed at increasing the external surface area. Architectures increase in volume by increasing in length: no scaling effect is therefore involved.

Figure 15 shows elementary patterns of both the optimised multi-airgap actuator and split-coil actuator.

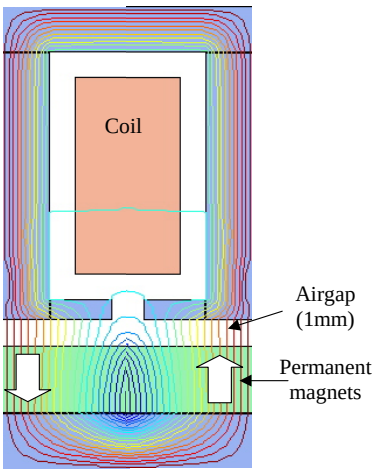

Fig. 15a: Optimised multi-motor architecture

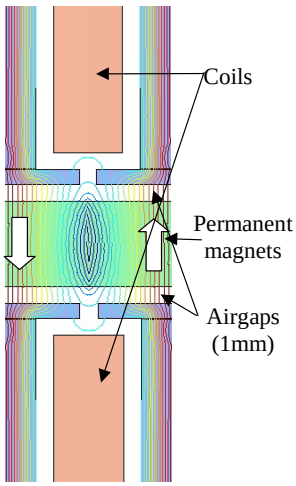

Fig. 15b: Optimised split-coil multi-airgap architecture

4.3 OPTIMISATION OF THE GLOBAL-COIL ARCHITECTURE

In this instance, cooling conditions change with dimensions. The current density changes inside the global coil: a scaling effect can therefore be observed.
We can however determine the optimised variable as a function of global volume, as follows:

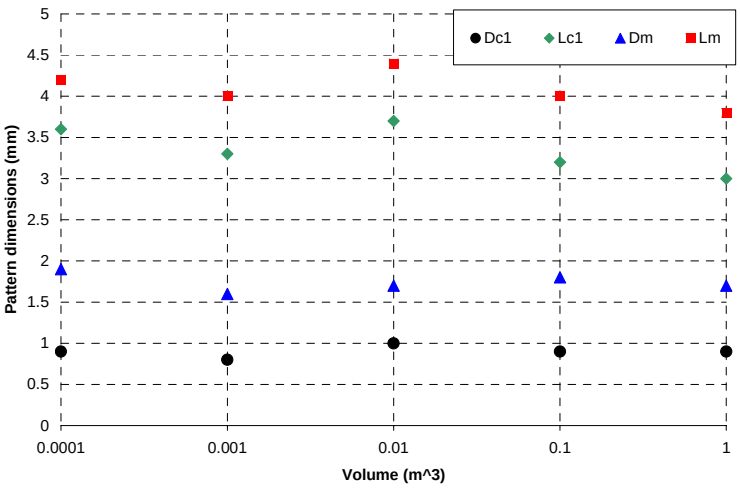

Fig. 16a: Optimised dimensions for the global-coil multi-airgap actuator as a function of global volume

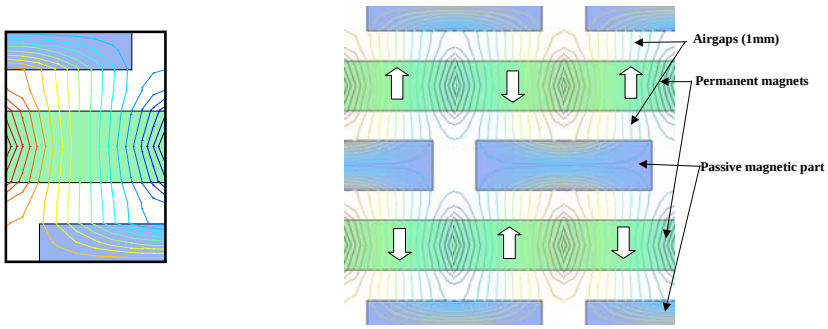

Fig. 16b: Optimised elementary pattern of a global-coil multi-airgap actuator and detail of the optimised actuator in conjunction

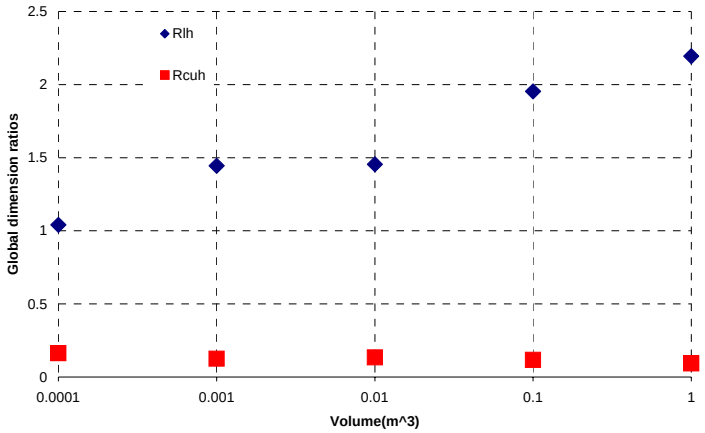

Fig. 16c: Global dimension ratio for the global-coil multi-airgap actuator as a function of global volume

One main finding from the global-coil optimisation is that the overall shape does not depend on global volume:

- Global coil-optimised actuators demonstrate a length-to-height ratio of around 2.5, which reflects a compromise between effective cooling conditions (i.e. more current) and the number of elementary patterns in parallel (i.e. increase in both flux and EMF).
- The other finding is that local dimensions do not depend to a great extent on global dimensions. We can thus speak of an “optimised elementary pattern”.

4.4 ARCHITECTURE COMPARISONS

The first architecture comparison consists of assessing the force as a function of volume under the previous conditions (see Section 4.1).

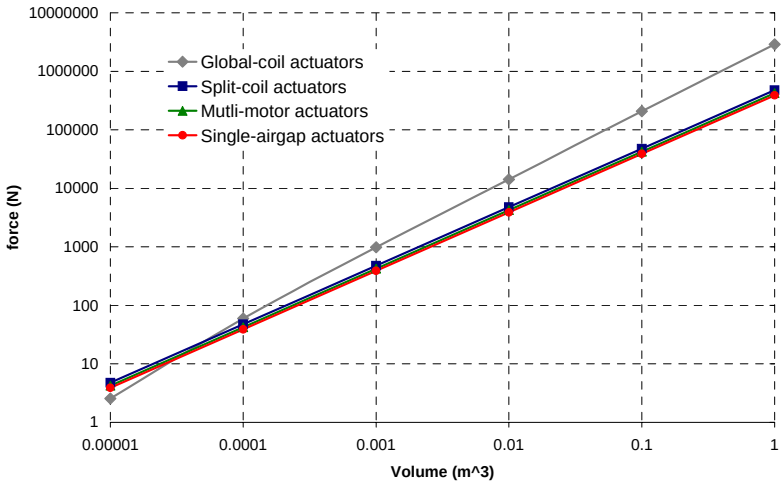

Fig. 17: Evolution of force as a function of volume

At this point, we can observe that for all architectures, force increases with volume. The split-coil architecture performs slightly better than the multi-motor architecture in this regard.
Moreover, for large volumes, global-coil architectures yield the highest force; on the other hand, for small volumes, performances are similar.

The force-volume ratio comparison is shown in the figure below:

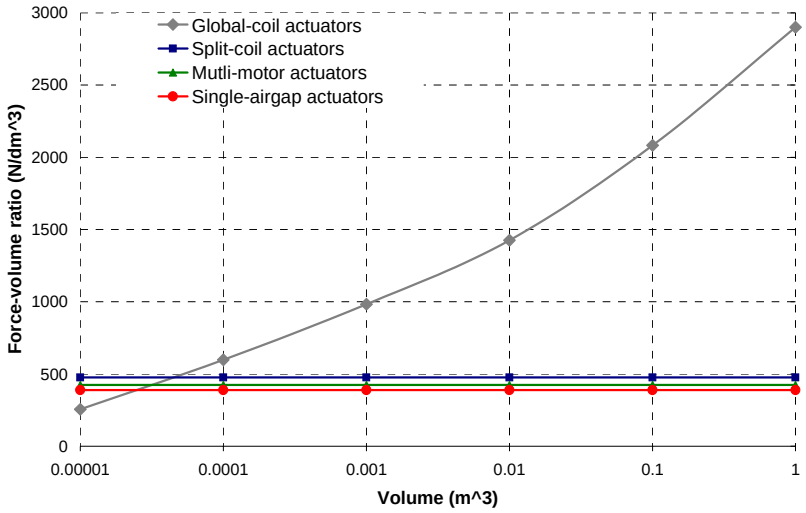

Fig. 18a: Evolution of the force-volume ratio as a function of volume for a thermal dissipation coefficient $ke = 10W.K^{-1}.m^{-2}$

These curves demonstrate that the force-volume ratio is constant for classical architectures; this finding stems from the fact that the actuators are primarily limited by thermal considerations. For very small volumes, the global-coil architecture is penalised by the longitudinal flux and exhibits a poorer force-volume ratio than classical architectures. However, once the thermal constraint becomes significant, the global-coil architecture yields far better results.

Under improved external cooling conditions, all actuators enhance their level of performance. On the one hand, the global-coil actuator raises its magnetic limitation, with pattern dimensions depending on global volume. On the other hand, classical actuators are penalised by the high thermal resistance of the insulator.

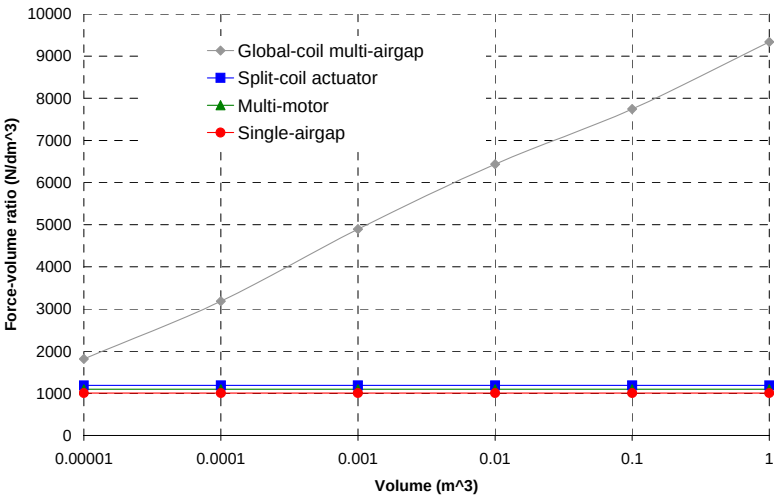

Fig. 18b: Evolution of the force-volume ratio as a function of volume for a thermal dissipation coefficient $ke = 100W.K^{-1}m^{-2}$

5. THE SCALING EFFECT IN GLOBAL-COIL MULTI-AIRGAP ACTUATORS

5.1 INTRODUCTION OF THE SCALING EFFECT IN CLASSICAL ACTUATORS

The scaling effect is used during quick comparisons of different kinds of actuators. The basic idea herein is to derive a set of laws, as realistic as possible, to provide the evolution in actuator performance as volume changes.
In the classical linear permanent-magnet actuators, it has been shown that [9]:
- under constant thermal conditions, the mechanical power is:

$$P_{mec} = F.v \propto H^{3.5}.\omega$$

where F is the force, V the mechanical speed, H an actuator dimension, and ω the electrical pulsation (which is held constant).

The approach then consists of applying the same method to our global-coil multi-airgap actuators.

5.2 SIZING HYPOTHESES

Thanks to the results from Section 4, we can develop a set of design rules for these global-coil actuators:

- Optimal pattern dimensions do not change considerably with global dimensions and thermal conditions ($R_{LH} \propto 1$ or $L \propto H$).
- The copper volume-to-global volume ratio does not change with global dimensions and thermal conditions either ($R_{cu_H} \propto 1$ or $Dcu \propto H$).
- Optimal pattern dimensions are directly proportional to the airgap g ($Dc1 \propto g$, $Lc1 \propto g$, $Lm \propto g$, $Dm \propto g$), which implies that for an airgap half the size, the optimised step is also cut in half ($\tau \propto g$).

These simple hypotheses are made possible by virtue of the optimised flux-M.M.F. diagrams for each pattern being slightly saturated.

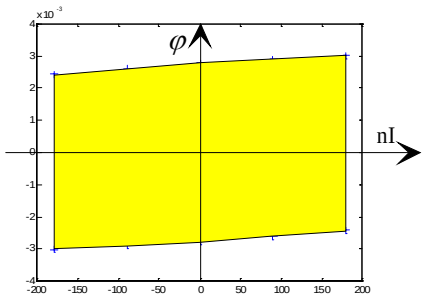

Fig. 19: A flux-M.M.F. diagram for an optimised pattern

We can now apply the equation in (5):

$$Wm = k.\varphi_m.mmf_{\max}$$

with:

$k = 4$ (ideal square-wave current)

$\varphi_m \propto h.w \propto g^2$

$mmf_{\max} = \dfrac{MMF_{\max}}{Ns}$, where $mmf_{\max}$ is the maximum magneto-motive force per pattern and $MMF_{\max}$ is the maximum total magneto-motive force:

$$W_m \propto \frac{g^2.MMF_{\max}}{Ns} \qquad (9)$$

5.3 THE SCALING EFFECT FOR GLOBAL-COIL MULTI-AIRGAP ACTUATORS

The square section provides the relation:	H = W	(10)
The total volume is:	$V = H.W.L \propto H^3$	(11)
The coil surface area is:	$S_{cu} \propto Dcu.L \propto H^2$	(12)
The pattern numbers in parallel are:	$N_p \propto \frac{H}{h}.\frac{W}{w} = \frac{H^2}{g^2}$	(13)
and in series are:	$N_s \propto \frac{L}{l} = \frac{H}{g}$	
The copper losses yield:	$P_{cu} \propto .Vcu.j^2$	(14)
	$V_{cu} \propto W.Scu = H^3$	(15)
	$P_{cu} \propto H^3.j^2$	(16)
The thermal model yields:	$P_{cu} \propto \gamma_{th}.\Delta T.S_{th}$	(17)
	$S_{th} = 2.L.W + 2.H.W \propto H^2$	(18)
	$P_{cu} \propto \gamma_{th}.H^2$	(19)
The current density is:	$j \propto \gamma_{th}^{0.5} H^{-0.5}$	(20)
The total magneto-motive force then is:	$MMF_{\max} \propto j.S_{cu} \propto \gamma_{th}^{0.5}.H^{1.5}$	(21)
The flux magneto-motive force diagram gives:	$W_m \propto g^3.\gamma_{th}^{0.5}.H^{0.5}$	(22)
The total force (see Equation 4):	$\overline{F} = N_p.N_s.\frac{W_m}{\tau} \propto \frac{\gamma_{th}^{0.5}.H^{3.5}}{g}$	(23)
For global-coil multi-airgap actuators, the force-volume ratio can be expressed as:	$\frac{\overline{F}}{V} \propto \frac{\gamma_{th}^{0.5}.H^{0.5}}{g}$	(24)

5.4 COMPARISON BETWEEN THE THEORETICAL SCALING EFFECT AND OPTIMISED ACTUATOR PERFORMANCE FOR GLOBAL COIL ACTUATORS

The evolution in force-volume ratio as a function of volume is illustrated in the following figure:

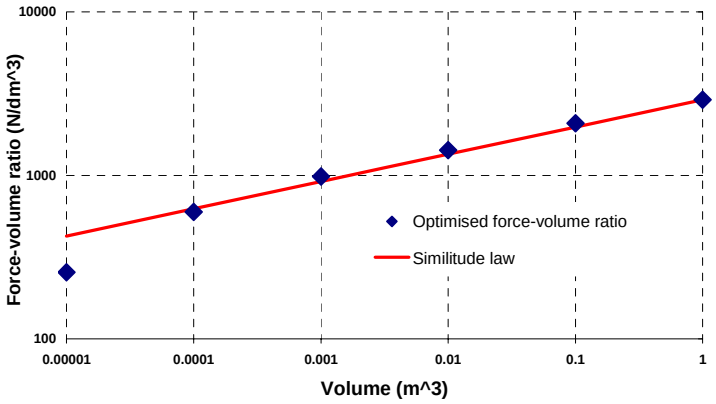

Fig. 20a: Comparison between the scaling effect and optimised architecture
For for different volumes (g = 1 mm, λ_{th} = 10 W.K^{-1}.m^{-2})

Except for very small and very large volumes, the scaling effect closely follows the values obtained through optimisation.
For the airgap value (1 mm) and cooling conditions, we can once again display the scaling effect and optimised actuator performance.

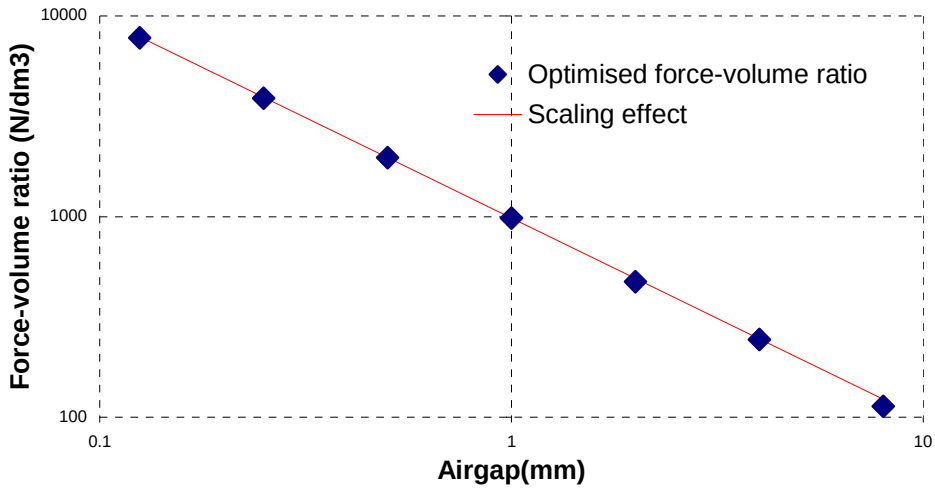

Fig. 20b: Comparison between the scaling effect and optimised architecture for different airgaps (V = 1 dm^3, ke = 10 $W.K^{-1}.m^{-2}$)

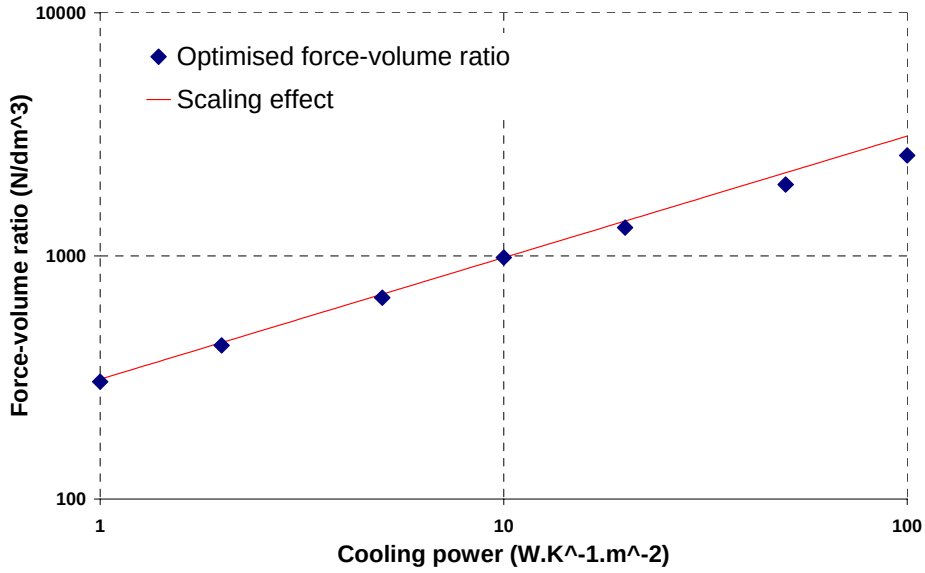

Fig. 20c: Comparison between the scaling effect and optimised architecture for different cooling powers (V = 1 dm^3, g = 1 mm)

We can conclude that this scaling effect law (24) is very accurate as long as the parameter remains within a reasonable range.

If the current density were to become very high (Equation 20) with either sizeable global dimensions or very good cooling conditions, the saturation effect would slightly modify the optimised patterns and the scaling effect would then be less accurate.

5.5 EXAMPLE OF A GLOBAL-COIL MULTI-AIRGAP ACTUATOR

An example of such a structure is displayed in Figure 21 below.

Fig. 21a: Positive conjunction

Fig. 21b: Negative conjunction

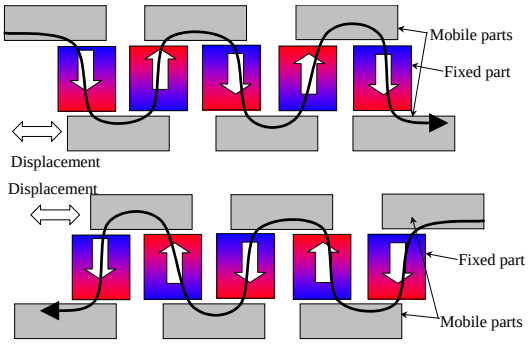

Fig. 21: Elementary cell of the multi-airgap actuator

This actuator features fixed permanent magnets of the NdFeB type with an induction of 0.65 T and a longitudinal field [5]. The mobile part is composed of magnetic blocks. Both the permanent magnets and winding are fixed on the stator.

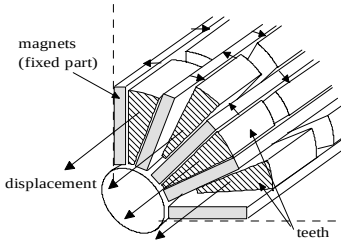

Fig. 22a: Composition of the active part of the actuator

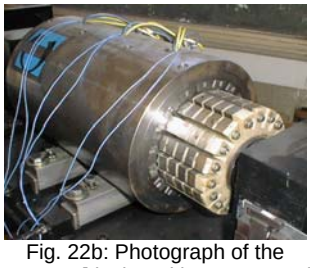

Fig. 22b: Photograph of the actuator [designed by LESIR and manufactured by Radio-Energy]

Fig. 22: Example of a permanent magnet reluctance multi-airgap actuator

This structure contains 36 airgap surfaces. The path is 55 mm long with a tooth step of 13 mm. Simulations have been conducted in order to compare simulations and measurements:

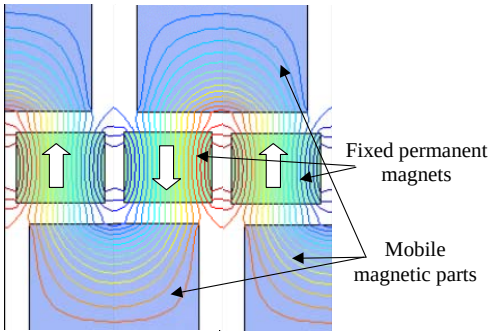

Fig. 23a: Finite Element Method simulation of an elementary pattern

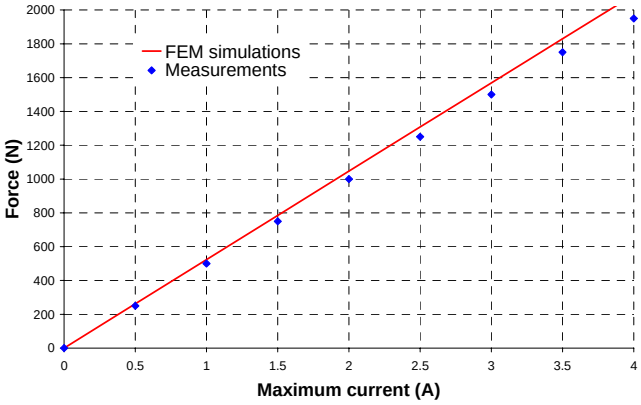

Fig. 23b: Comparison between F.E.M. simulations and measurements under airflow cooling conditions

We can note that the finite element method very closely follows the measured force, which means that the optimisation model is quite accurate. However, the global-coil multi-airgap prototype features an elementary pattern that substantially differs from the optimal shape depicted in Figure 16. This is mainly due to mechanical constraints (permanent magnet minimum width, number of airgaps, etc.). Moreover, the active part is not being very well utilised. Hence, performances are lower than those of the optimal actuator.

When operating in impulse mode (i.e. without any heat limit), this actuator generates a thrust of 24,000 N. The airgap is equal to 1.2 mm and the active volume is 9.6 dm^3 for a peak force-volume ratio of 2,500 N/dm^3.
We can now compare this force-volume ratio with the optimal performances obtained under good cooling conditions (see Fig. 18b). On this same figure, we have represented the optimal performance with single-airgap architecture, as well as performances of the best commercial linear actuators [10],[11].

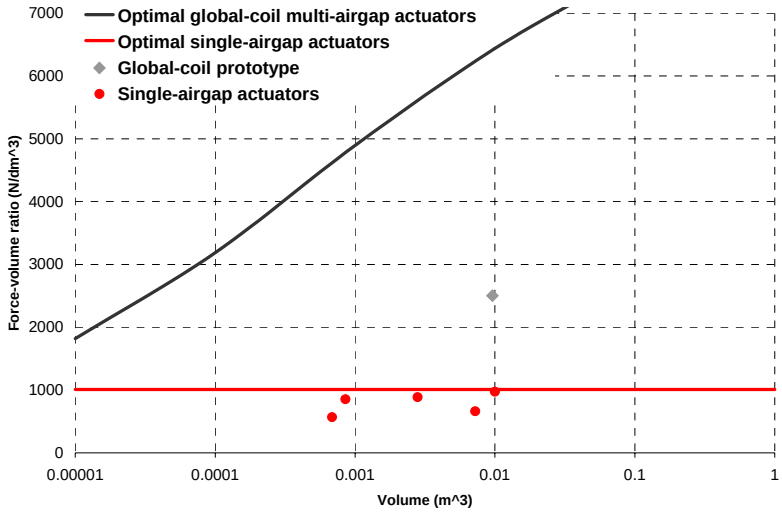

Fig. 24: Comparison of scale effect between optimisation results and actual actuators

For single airgap architectures, optimal actuators performances are rather close from real actuators performances. For global coil actuators, the optimal values are more than twice as high as those of actual actuators. This is mainly due to mechanical constraints, which we have neglected in our study. Nonetheless, global-coil actuator performance remains very attractive in comparison with classical linear actuators.

6. CONCLUSION

In this paper, a comparison of the evolution in force density as a function of actuator volume for various types of linear actuator architecture has been conducted. The study has served to highlight the advantage of multiplying the number of airgap surfaces in the case of global-coil architecture.
An example of an actuator featuring an original design and a high force-volume ratio was also presented.

These results still depend however on the mechanically-feasible rate of active zone-splitting. As such, the obstacles involved in this development process merit specific mention, namely:

- the production of magnetic blocks and small-sized magnets, including their assembly;
- mechanical precision, in order to attain a small mechanical gap in comparison with the structure's overall dimensions;
- guidance of several mobile parts over long paths;
- compensation for the high normal bonding stresses associated with the eccentricity of mobile parts, with respect to fixed parts.

This study has been carried out for low-speed movement, in which iron losses are neglected. For higher speeds, a new optimisation procedure would have to be implemented.

7. REFERENCES

[1] Rioux C., « Théorie générale comparative des machines électriques établie à partir des équations du champ électromagnétique », *R.G.E.* - May 1970 - Tome 79, N° 5, pp. 415-421.

[2] Ben Ahmed H., Prévond L., Multon B., Salamand B. and Lucidarme J., "Special Synchronous *Linear Actuators: Structures and Performances", Electromotion Revue, 5, oct. 98., pp. 93-101*.

[3] Cavarec P.E., Ben Ahmed H. and Multon B., "Advantage of Increasing the Number of Airgap Surfaces in Synchronous Linear Actuators", Electromotion 2001, June 19-20, 2001, Bologna, Italy, pp. 251-256.

[4] Bolognesi P. and Taponecco L., "Analysis of an unconventional linear PMAC machine suitable for reciprocating motion generation systems", Electromotion 2001, June 19-20, 2001, Bologna, Italy, pp. 443-448.

[5] Desesquelles P.F., Lucidarme J. and Ben Ahmed H., "Theoretical and Experimental Results Upon Multi-Airgap Axial Synchronous Machines With Permanent Magnets", *ICEM'90*, Cambridge Mass. (USA), August 1990.

[6] Amiet M. and Lucidarme J., « Accélérateur ou actionneur linéaire », *French patent, filed by the State*, N° 95 15703, December 1995.

[7] Matt, Goyet R., Lucidarme J. and Rioux C., "Longitudinal Field Multi-Airgap Linear Reluctance Actuator", *Electric Machines & Power Systems*, 1987, 13:299-313.

[8] Staton D., Soong W. and Miller T.J., "Unified theory production in switched reluctance and synchronous reluctance motors", IEEE Transactions on Industry Applications, Vol. 31, March-April 1995.

[9] Jufer M., "Electromécanique", Traité d'électricité, collection EPFL, Vol. IX, Chapter 4.

[10] Avcon Inc. (US) http://www.calinear.com

[11] Etel S.A. (CH) ML 2020. http://www.etel.ch/